Green Chemistry

ROYAL SOCIETY OF CHEMISTRY

PAPER

View Article Online
View Journal | View Issue

Cite this: *Green Chem.*, 2025, **27**, 2117

NiFeCo wrinkled nanosheet electrode for selective oxidation of 5-hydroxymethylfurfural to 2,5-furandicarboxylic acid†

Bingkun Chen,[a] Bowen Yang,[b] Yaqiong Su,[c] Qidong Hou,[b] Richard Lee Smith, Jr,[d] Xinhua Qi *[b] and Haixin Guo *[a]

Quantitative and selective oxidation of 5-hydroxymethylfurfural (HMF) to 2,5-furandicarboxylic acid (FDCA) *via* electrocatalysis is a crucial milestone for biomass conversion. In this study, FeCo-modified β-$Ni(OH)_2$ wrinkled nanosheet electrode were prepared by a hydrothermal method and used for the electrocatalytic oxidation of HMF to afford 100% conversion, 98.7% FDCA yield and a Faraday efficiency (FE) of 98%. The wrinkled nanosheet structure design increased the surface area (26.3 $m^2\ g^{-1}$) and introduced oxygen-rich active sites (35.26%), enabling a current density of 10 mA cm^{-2} for HMF oxidation at 1.26 V *vs.* RHE. *In situ* electrochemical characterization established that β-NiOOH was the actual oxidation active site. The decoration of FeCo promoted the formation of β-NiOOH species, in which Ni^{3+} was converted into Ni^{2+} *via* the hydroxy and aldehyde groups in HMF, while HMF was dehydrogenated to the oxidative derivative (FDCA) at the anode. Electrochemical cyclic voltammetry confirmed that the substrate and product species followed a Langmuir–Hinshelwood (L–H) adsorption mechanism. Density functional theory (DFT) calculations verified that the Gibbs free energy and adsorption energy of HMF can be adjusted through the co-doping of the FeCo composition, which was more effective in capturing protons and electrons and activating HMF. This work lays the foundation for a deeper understanding of polymetallic site synergies and provides a practical technique for the upgrading of electrochemical substance derivatives into structural unit chemicals.

Received 19th November 2024,
Accepted 10th January 2025

DOI: 10.1039/d4gc05911e

rsc.li/greenchem

Green foundation

1. The oxidation of biomass-derived furans to 2,5-furandicarboxylic acid (FDCA) holds significant implications for achieving the UN Sustainable Development Goals. This is because FDCA has a substantial future as a monomer for bio-based polymers. Our work promotes green chemistry as it enables the efficient electrocatalytic oxidation of HMF to FDCA, replacing traditional thermal catalysis and contributing to Goal 7 by reducing the consumption of non-renewable energy sources.
2. The catalyst is prepared by a hydrothermal method in water. It achieves 100% HMF conversion, 98.7% FDCA yield, and 98% Faraday efficiency. It exhibits a low overpotential (157 mV) and a high current density (66.2 mA cm^{-2}) at 1.5 V *vs.* RHE. The nickel leaching of the catalyst is less than 0.002 ppm after each cycle.
3. Future research will focus on replacing or minimizing the use of inorganic bases.

[a]*Agro-Environmental Protection Institute, Chinese Academy of Agricultural Sciences, No. 31, Fukang Road, Nankai District, Tianjin, 300191, China.*
E-mail: haixin_g@126.com
[b]*College of Environmental Science and Engineering, Nankai University, No. 38, Tongyan Road, Jinnan District, Tianjin, 300350, China.*
E-mail: qixinhua@nankai.edu.cn
[c]*School of Chemistry, Engineering Research Center of Energy Storage Materials and Devices of Ministry of Education, National Innovation Platform (Center) for Industry-Education Integration of Energy Storage Technology, Xi'an Jiaotong University, Xi'an, 710049, China*
[d]*Graduate School of Environmental Studies, Tohoku University, Aramaki Aza Aoba 468-1, Aoba-ku, Sendai, 980-8572, Japan*
† Electronic supplementary information (ESI) available. See DOI: https://doi.org/10.1039/d4gc05911e

1. Introduction

Conversion of renewable resources using sustainable chemistry has shown great progress in platform chemical production and energy systems.[1,2] The priority chemical 2,5-furandicarboxylic acid (FDCA) can be synthesized from 5-hydroxymethylfurfural (HMF)[3,4] and has considerable potential as a monomer for bio-based polymers.[5,6] Although FDCA can be obtained from HMF *via* thermal catalysis or biocatalysis, these methods often require severe reaction conditions, long reaction times, or energy-intensive separations.[7] Electrocatalytic oxidation of HMF for FDCA production, on the other hand, requires low energy consumption and operates under relatively mild conditions, making it a promising approach for renewable resource transformation schemes.[8,9]

Development of electrocatalytic electrodes that are selective for oxidation is necessary for realizing HMF conversion on a commercial scale. In general, because precious metals are limited in their application due to cost and stability, research has focused on transition metal catalysts, including hydroxides,[10] oxides,[11] phosphides,[12,13] nitrides,[14] and sulfides[15] of transition metals (Ni, Fe or Co). For the HMF oxidation reaction (HMFOR), Ni-based compounds are thought to be among the most prospective non-noble metal catalysts,[16] but their low conductivity and intrinsic electronic structure require a high potential to begin the reaction. Therefore, the construction of efficient, fast charge transfer, and cheap electrocatalytic materials is an ideal choice to achieve low-cost preparation of FDCA. It has been demonstrated that layered double hydroxides (LDH), which are typically two-dimensional materials made up of cationic plates with hydroxyl groups and interlayer anions with modifiable compositions, are effective candidates for the oxidation of small molecules such as water, methanol, and HMF.[17,18] To improve electrocatalytic activity, constructing multiple sites to form synergies between trimetallic centers is an effective strategy. Transition metals such as Co, Fe, and Mn incorporated into nickel-based oxides or hydroxides to synthesize ternary composite materials can modulate the electronic structure of layered double hydroxides (LDHs) and significantly enhance their electrocatalytic performance in HMF oxidation.[19] Nanosheet structures of layered double hydroxides (LDHs) containing transition metals have moderate specific surface areas (26 $m^2\ g^{-1}$) and relatively high turnover frequencies (0.44 s^{-1}), which can provide effective charge transfer channels for electrolysis reactions.[20]

By adjusting the Ni/Co ratio, Niu *et al.* synthesised a range of $Ni_xCo_{3-x}O_4$ catalysts and verified the contribution of Ni species to kinetic enhancement and the cooperative catalytic impact of Co incorporation. However, the synergies of multiple metal species in catalytic processes and the intrinsic mechanisms governing the electron structure of Ni-based electrocatalysts and composites remain unclear. Liu *et al.* considered that the true active species for HMFOR are the developed high-valence species (β-NiOOH) of $Ni^{2+\delta}$.[21] From the current viewpoint, it remains uncertain whether doped polymetals contribute to HMF oxidation in a complementary way or whether the sub-centre merely modifies the electronic structure of the primary center. Therefore, elucidating the actual impacts of Ni–Fe–Co sites on catalytic activity and selectivity is imperative. Additionally, the binding and absorption of OH– comprise a key factor influencing HMFOR as they are crucial for the formation of high-value activation phases or the activation of C–H/O–H nodes.[22–24] However, the adsorption process of OH^- on the catalyst surface in the electrocatalytic oxidation of HMF has not been found.

In this work, an electrocatalyst with an FeCo-decorated β-Ni $(OH)_2$ nanosheet array structure grown *in situ* on NF was synthesized and the oxidation mechanism of NiFeCo-LDHs for HMFOR was studied. The effects of polymetallic site construction on electrocatalytic HMF oxidation were examined by comparing the properties of NiFe-LDHs, NiCo-LDHs and NiFeCo-LDHs. *In situ* spectrum and electrochemistry techniques were utilized to explore the absorption and coupling mechanisms of catalysts for organic molecules and OH^- in alkaline environments. The differences between the Eley–Rideal (E–R) and Langmuir–Hinshelwood (L–H) mechanisms in active sites and adsorption groups were investigated. The adsorption behavior and dehydrogenation free energy of HMF oxidation were analyzed utilizing density functional theory (DFT). The partial state density (PDOS) at the Fermi level, the crystal orbital Hamilton population (COHP) and the charge density difference (CDD) were also calculated to elucidate the synergistic effect of multiple metal sites, the regulation of the electronic structure and the activation of HMF by co-doping. Combined with electrochemical experiments, this work highlights the engineering of electronic structures in NiFeCo-based hydroxides for HMFOR from the perspective of multi-metal site synergies.

2. Results and discussion

2.1. Characterization of the samples

The catalyst preparation process is given in Fig. 1a. The hierarchical NiFeCo-LDH nanoarrays formed by multiple metal ions (Ni^{2+}, $Co^{2+}$and Fe^{2+}) grew *in situ* vertically on the exterior of the NF, according to the NiFeCo-LDH scanning electron microscope image (Fig. 1b). A densely grown array of hierarchical nanosheets covered the nickel foam surface, as shown in the SEM image (Fig. 1c). These dense and ultra-thin nanolayers most likely increase the specific surface area as shown next. A type-IV isotherm of an adsorption–desorption hysteresis loop, which is a feature of mesoporous structures, was observed in the prepared samples (Fig. S1†). The specific surface area (26.3 $m^2\ g^{-1}$) and mesopore volume (0.33 $cm^3\ g^{-1}$) of NiFeCo-LDHs were greater than those of NiFe-LDHs and NiCo-LDHs (Table S1†), indicating that the metal interactions affected the structural properties of the materials. The addition of iron was essential for forming hierarchical nanoarray structures. NiFe-LDHs and NiFeCo-LDHs had similar morphologies, but NiCo-LDHs were single-layered nanosheet structures (Fig. S2†). NiFeCo-LDH nanoarrays with several folds

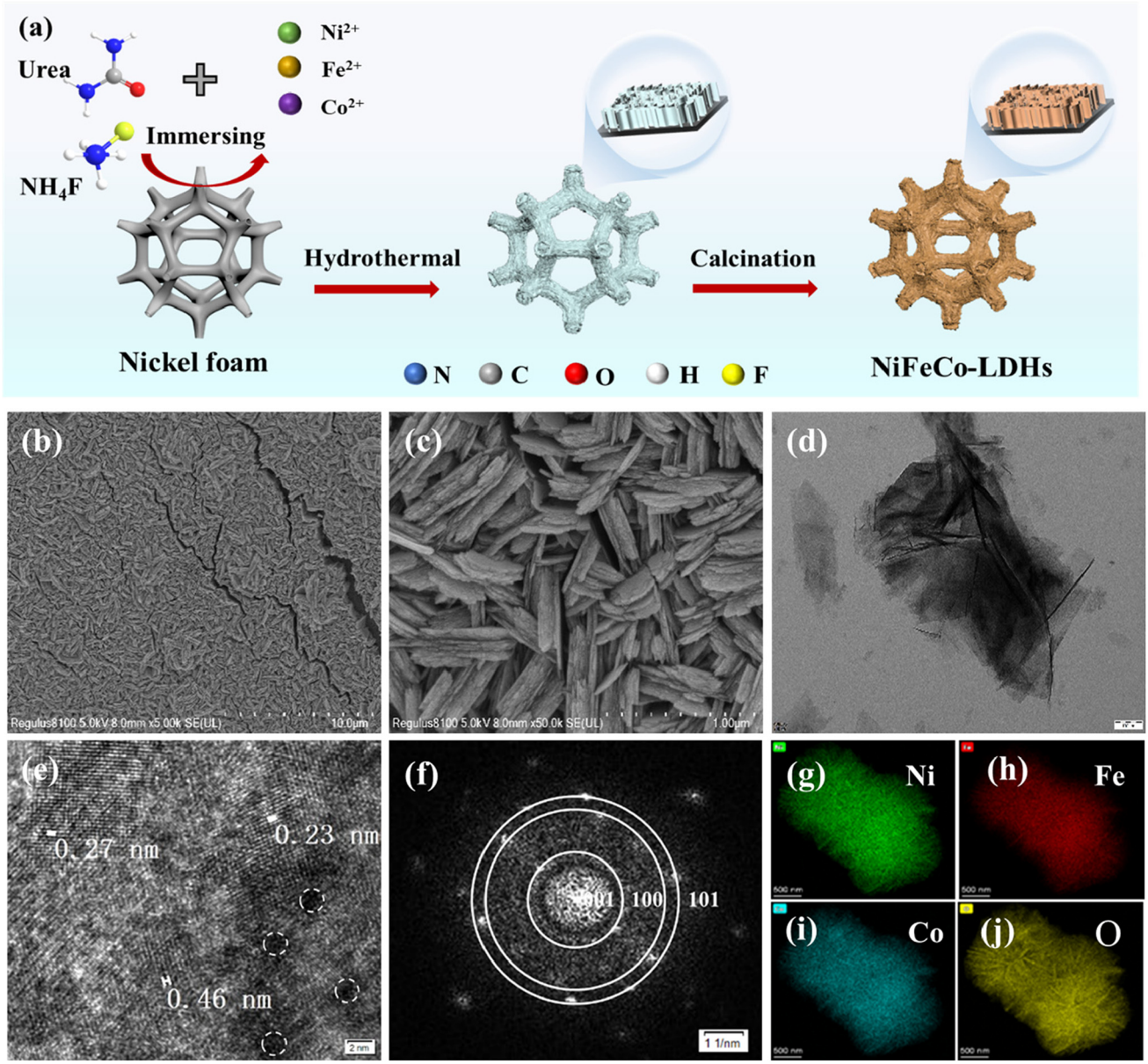

Fig. 1 (a) Schematic illustration of preparation; (b) SEM image of NiFeCo-LDHs in low and (c) magnified resolution; (d) TEM image of the NiFeCo-LDHs; (e and f) HRTEM and SAED images; and (g–j) elemental maps of the NiFeCo-LDHs.

were additionally revealed by transmission electron microscope images (Fig. 1d). The crystalline nickel hydroxide undergoes four crystal transformations during the electrochemical reaction, namely α-$Ni(OH)_2$, β-$Ni(OH)_2$, β-NiOOH, and γ-NiOOH. When β-$Ni(OH)_2$ is the active substance, in the normal charge and discharge process, the nickel electrode reaction occurs between β-$Ni(OH)_2$ and β-NiOOH. Bode *et al.*[25] found that the charge–discharge reaction between α-$Ni(OH)_2$ and γ-NiOOH can take place simultaneously with the β → β reaction, so γ-NiOOH can be discharged to form α-$Ni(OH)_2$. Nevertheless, α-$Ni(OH)_2$ is highly unstable in alkaline solutions and is readily converted to β-$Ni(OH)_2$. Additionally, studies have demonstrated that when preparing $Ni(OH)_2$, adding an appropriate amount of metal ions such as Co can inhibit the transformation of $Ni(OH)_2$ to the γ-type during overcharging, thereby enhancing the utilization rate of the active substances.[26] The HRTEM and SAED images (Fig. 1e and f) showed clear lattice fringes and diffraction patterns with lattice spacings of 0.46, 0.27, and 0.23 nm, respectively. These spacings correspond to the (001), (100), and (101) planes of β-$Ni(OH)_2$.[27] The HR-TEM image of NiFeCo-LDHs (Fig. 1e) clearly showed hazy areas (circle area), which may have resulted from the lattice deformation caused by oxygen vacancies.[28] The element mapping illustrated that the Ni, Co and Fe elements were uniformly distributed within the nanosheets (Fig. 1g–j).

The components Ni, Fe, Co, and O were present in the respective samples as indicated by the XPS spectra of NiFeCo-LDHs, NiFe-LDHs, and NiCo-LDHs (Fig. S3†). The XPS spectra of NiFeCo-LDHs exhibited two characteristic peaks at 873.6 eV and 855.8 eV, which correspond to Ni $2p_{1/2}$ and Ni $2p_{3/2}$ (Fig. 2a). Two satellite peaks at 879.3 eV and 861.1 eV were also observed, consistent with the existing literature.[29,30] The binding energies of Fe $2p_{3/2}$ and Fe $2p_{1/2}$ exhibited by the two main peaks in the Fe 2p XPS spectrum (Fig. 2b) were found at 719.1 and 711.5 eV, respectively, aligning with the reported values.[31] The spectrum of Co 2p in Fig. 2c was assigned to two spin-orbiting doublets. The peaks at 780.5 eV and 796.7 eV corresponded to Co $2p_{3/2}$ and Co $2p_{1/2}$, with associated satellite peaks identified at 785.3 eV and 802.8 eV, respectively. The presence of Co^{3+} and Co^{2+} was verified by the peaks at 776.3 eV and 780.5 eV in accordance with the literature.[32] Notably, the binding energies of Ni 2p, Fe 2p and Co 2p for NiFeCo-LDHs shifted slightly to higher binding energies (0.4–1.3 eV) when compared with NiFe-LDHs and NiCo-LDHs, demonstrating that Ni, Co, and Fe have electronic interactions.[33] This suggested that Ni, Fe and Co were introduced into the nickel foam as intended and that they changed the original electronic structure, so as to improve the adsorption energy of the intermediate on the electrode. With FeCo co-doped, the Ni content of NiFeCo-LDHs (19.7%) increased compared with NiFe-LDHs (14.8%) and NiCo-LDHs (15.4%) (Table S2†). It is known that FeCo doping enhances metal–support interactions, promotes the distribution of Ni, and produces an amount of active site precursors (β-$Ni(OH)_2$).[34] In addition, the high-resolution O 1s XPS spectra of samples clearly revealed the three deconvoluted main peaks of O_1 (529.7 eV), O_2 (531.8 eV), and O_3 (534.1 eV) (Fig. S11, ESI†), corresponding to the metal–oxygen bond, defect oxygen, and adsorbed oxygen, respectively.[35] As reported before, there was a positive relationship between the O_2 ratio and the V_O density.[36] The larger intensity ratio of the defect oxygen peak for NiFeCo-LDHs (35.3%) with respect to that of NiFe-LDHs (20.6%) or NiCo-LDHs (31.41%) further confirmed that the polymetallic coordination create more unpaired electrons to increase the V_O concentration. The use of NH_4F enhanced the catalyst stability and inhibited metal (Ni) leaching. The presence of F was detected in XPS, which can shorten the M–O(F) bond length, thus increasing the bond energy, and improving crystal structural stability (Fig. S11b†).[37] Fluorine raises the migration barrier of transition metals (Ni) during the electrochemical reaction process and inhibits or decelerates the dissolution of transition metals.[38] The ICP analysis results demonstrated that the leaching of Ni was less than 0.002 ppm after each cycle, indicating that the synthesized catalyst was stable under the reaction conditions. Moreover, although 0.001 mol of NH_4F was used in this work, we are currently striving to identify substitutes for NH_4F.

The crystal structure of the sample was analyzed using an X-ray diffractometer. The diffraction peaks for the sample

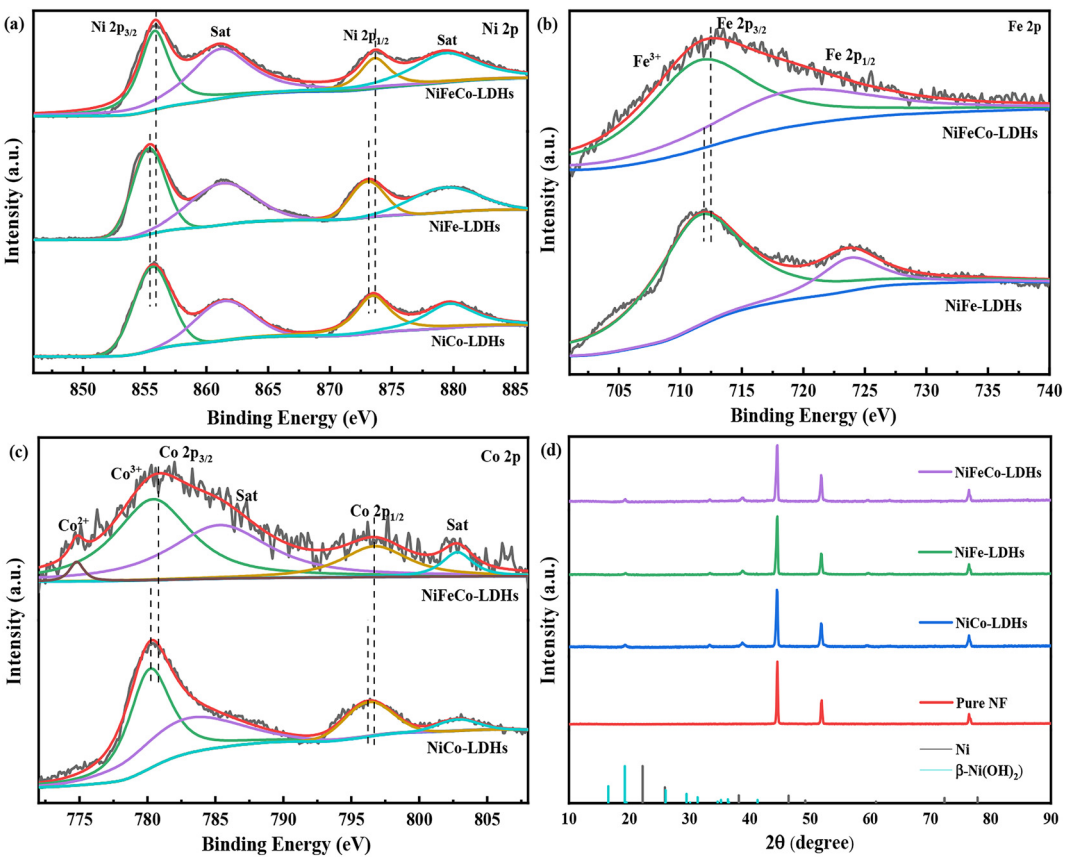

Fig. 2 XPS spectra of NiFeCo-LDHs: (a) Ni 2p, (b) Fe 2p and (c) Co 2p. (d) XRD patterns of NiFeCo-LDHs, NiFe-LDHs, NiCo-LDHs, and pure NF.

without the incorporation of Fe or Co were attributed to the nickel foam (PDF#04-0850) (Fig. 2d). There was a small diffraction peak for Ni, which can be attributed to the underlying Ni on the NF substrate. Upon introduction of Fe and Co, a β-Ni $(OH)_2$ phase was identified (PDF#14-0117). The observed diffraction peaks at 2θ values of 19.2°, 33.0°, 38.5°, 59°, and 62.7° corresponded to the hexagonal structure of β-Ni$(OH)_2$ with respective planes designated as (001), (100), (101), (110), and (111). The surfaces of the nanoarrays represented the (001) planes of β-Ni$(OH)_2$; however, it is noteworthy that the diffraction peak corresponding to the (101) crystal facets was more pronounced than that for the (001) plane. This discrepancy may be attributed to Ostwald ripening occurring along the (001) plane following initial growth along the (101) planes.[39] Doping with iron and cobalt ions facilitates partial replacement of nickel ions within the lattice structure of β-Ni $(OH)_2$; consequently, a large number of –OH groups can be adsorbed into this layer due to its single crystalline phase characterized by a closely packed atomic arrangement resulting from crystallization.[40] For Fe/Co-doped NF, there was no additional Fe or Co phases that could be recognized, indicating full Fe atom incorporation into the β-Ni$(OH)_2$ lattice, which may form NiFeCo solid solutions due to similar lattice characteristics.[41,42] However, a slight shift in the XRD peaks after Fe and Co doping was observed.

2.2. Electrocatalytic performance

In a three-electrode system utilizing a 1 M KOH electrolyte, the electrocatalytic performance of the synthesized catalysts was assessed through linear sweep voltammetry (LSV) curves. The HMFOR and OER capabilities of the fabricated hierarchical NiFeCo-LDHs nanoarrays are displayed in Fig. 3a. Compared with the reported Ni-based electrocatalysts, the hierarchical NiFeCo-LDH nanoarrays attained a current density of 10 mA cm^{-2} at 157 mV of overpotential in the absence of HMF (Table S3†). The onset potential of the hierarchical NiFeCo-LDH nanoarrays shifted negatively to 1.26 V *vs.* RHE upon the addition of 50 mM HMF to the electrolyte system. This observation indicates that, at low potentials, the HMFOR is more favorable than the OER. Compared with NiFeCo-LDHs, the current density of the original NF was lower, although it exhibited some electrocatalytic activity for the electrooxidation of HMF (Fig. 3b). NiFeCo-LDHs exhibited the best HMF electrocatalytic performance under alkaline conditions, and had a lower onset potential and higher current density than NiFe-LDHs, NiCo-LDHs and the original NF (Fig. 3c). The Tafel slopes for NiFeCo-LDHs, NiFe-LDHs, NiCo-LDHs and NF were (25.17, 30.03, 39.69 and 285.3) mV dec^{-1}, respectively. The low Tafel slope of NiFeCo-LDHs, in comparison with other materials, suggests a higher catalytic efficiency and faster dynamics on the electrode surface. Cyclic voltammetry (CV) was employed to determine the relative electrochemically active surface area (ECSA), thereby assessing the electrocatalytic activity of the electrode for HMF (Fig. S4†). Utilizing CV curves with a scan rate of (20–100) mV s^{-1} and a potential range of −0.1 to 0.1 V *vs.* RHE, the double layer capacitance (C_{dl}) was calculated. C_{dl} showed a positive correlation with the ECSA. Compared with NiFe-LDHs, NiCo-LDHs had a higher C_{dl} value and a higher electrochemically active surface area, while NiFeCo had a much higher C_{dl} value (70.84 mF cm^{-2}) than NiFe (26.2 mF cm^{-2}), NiCo (27.36 mF cm^{-2}) and NF (2.27 mF cm^{-2}). The ECSA of NiFeCo-LDHs, NiFe-LDHs, NiCo-LDHs and NF were (1771, 655, 684 and 56.75) cm^2, respectively, which indicates that the hierarchic structure of NiFeCo can improve the ECSA and expose more catalytic active sites compared with other materials (Fig. 3e). Within the conditions of 1.0 M KOH and 50 mM HMF, Liu *et al.*[43] prepared NiS_x-modified β-Ni $(OH)_2$ electrodes, and obtained a Tafel slope of 124 mV dec^{-1} and the maximum C_{dl} with 11.2 mF cm^{-2}. The electrode prepared in this work obtained a Tafel slope of 25.17 mV dec^{-1} and a C_{dl} of 70.84 mF cm^{-2}, which represents great progress compared with Liu *et al.*, indicating that the NiFeCo-LDH electrode constructed in this work had a fast reaction rate and a large electrochemical specific surface area.

The transfer coefficient (β), which can be found in the ESI (eqn (6)),† indicates the extent to which the change in electric potential affects the electrode activation energy or the response rate.[44,45] The transfer coefficients (β) of NiFeCo-LDHs, NiFe-LDHs, NiCo-LDHs and NF were 0.39, 0.32, 0.25 and 0.03, respectively, which revealed favorable catalytic properties for NiFeCo-LDHs. The intrinsic catalytic activity of the catalyst can be assessed using turnover frequency (TOF), which was determined as shown in the ESI (eqn (7), ESI†).[46,47] The TOF values of NiFeCo-LDHs, NiFe-LDHs, NiCo-LDHs and the precursor NF were 0.44 s^{-1}, 0.39 s^{-1}, 0.32 s^{-1} and 0.21 s^{-1}, respectively.

The interfacial properties of the catalysts were characterized with electrochemical impedance spectroscopy (EIS) for estimating the kinetics and electron transfer between the electrodes and the electrolyte (Fig. 3f). In a Nyquist diagram, the diameter of a semicircle equals R_t. In comparison with NiFe- or NiCo-LDHs, it was found that NiFeCo-LDHs had a minimum charge transfer resistance (R_t), indicating their capacity for faster electron transport at the electrode interface than the other materials prepared. It is worth noting that NiCo-LDHs had a higher C_{dl} value, but a larger impedance, than the other materials, which is not conducive to mass transfer, while NiFe-LDHs had high electrical conductivity. Doping Fe into the structures greatly reduced the electrochemical impedance of layered nanoarrays and increased the electrochemically active surface area. NiFeCo-LDHs exhibited a much smaller Nyquist semicircle diameter compared with the NiFe-LDHs, NiCo-LDHs and NF, which demonstrates that the charge transfer resistance was much smaller and had a faster electron transfer capability during the HMFOR.

2.3. Reaction pathway and stability of the catalyst

High-performance liquid chromatography (HPLC) was used to determine the dynamic changes and reaction progress of the HMFOR and oxidation products (Fig. 4a and Fig. S4†). The intensity of HMF steadily became lower with a rise in the reaction time, along with an increase in the FDCA intensity. After the HMF oxidation reaction, 100% HMF conversion, 98.7%

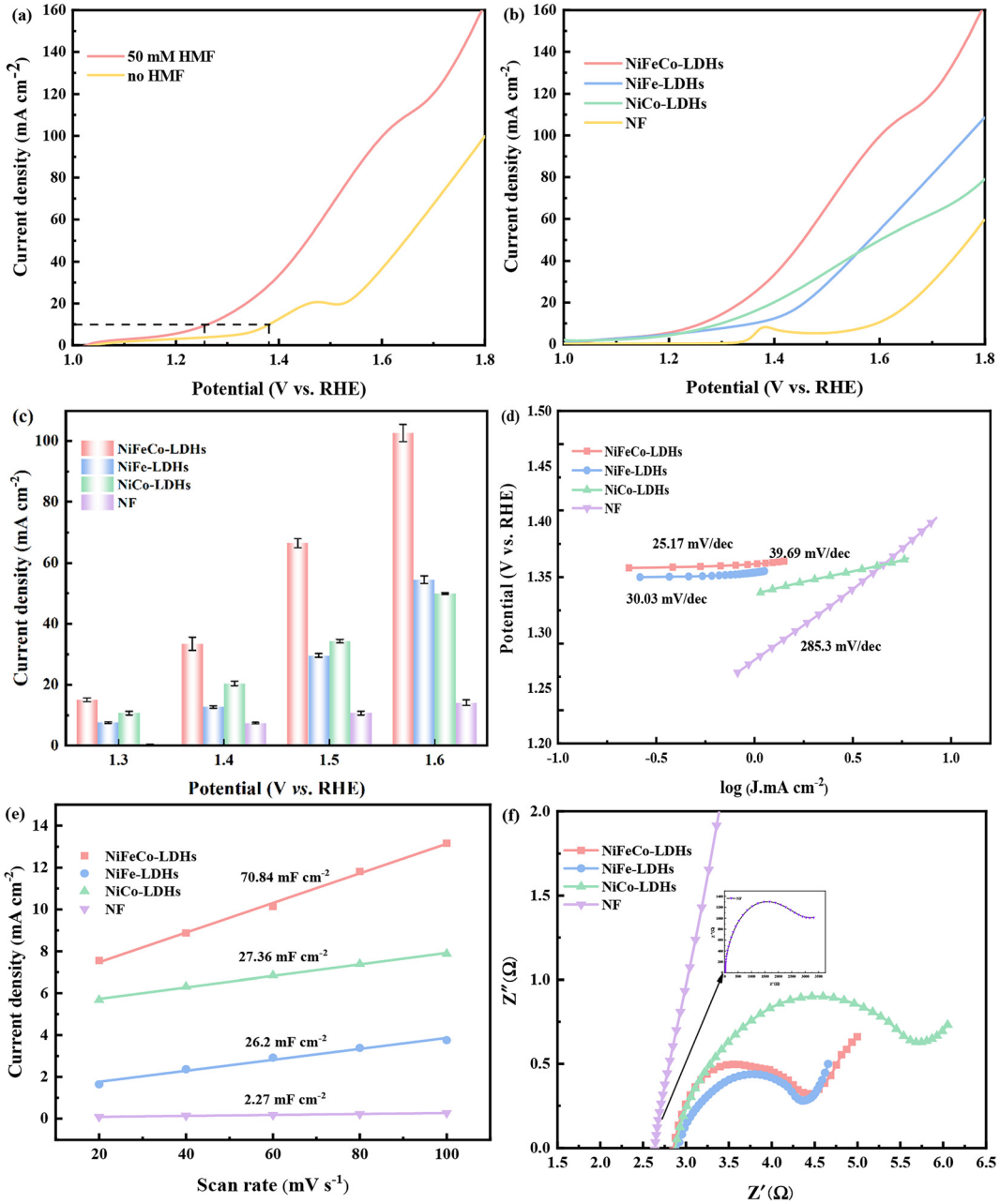

Fig. 3 (a) LSV curves of NiFeCo-LDHs (50 mM HMF/no HMF); (b) LSV curves of NiFeCo-LDHs, NiFe-LDHs, NiCo-LDH, and NF; (c) current densities at several potentials; (d) Tafel slopes of materials; (e) electrochemical surface area (ECSA); and (f) Nyquist plots of the electrodes.

FDCA yield and 98.0% Faraday efficiency (FE) were obtained, which were higher than the values reported in previous electrocatalyst studies (Fig. 4c and Table S4†). Layered pleated nanoarrays grew vertically and most likely facilitated ion diffusion, enhanced the availability of active sites and improved the structural stability in the electrolyte, thereby promoted HMFOR.[48] Notably, HPLC analysis revealed the existence of the intermediate HMFCA but not DFF, demonstrating that path I was taken by HMF during the electrooxidation process (Fig. 4b and e). Production of HMFCA increased slowly at first before decreasing, indicating that the oxidation of HMFCA to FFCA was the rate-determining step of the HMFOR in alkaline solution.[49] Chronopotentiometry measurements (*I*–*t*) were conducted at a constant potential of 1.50 V *vs.* RHE over a duration of 24 h to evaluate the stability of the NiFeCo-LDHs (Fig. S6a†). During the 24 h stability test, the current density of the NiFeCo-LDHs was preserved with a small decay in anodic current loss (about 6%). On the other hand, recycling experiments were carried out for the HMFOR using NiFeCo-LDHs at 1.5 V *vs.* RHE. After 5 cycles, the conversion rate of HMF, the yield of FDCA and FE were maintained at 99–100%, 91.6–98.7% and 96–98%, respectively (Fig. 4d). ICP

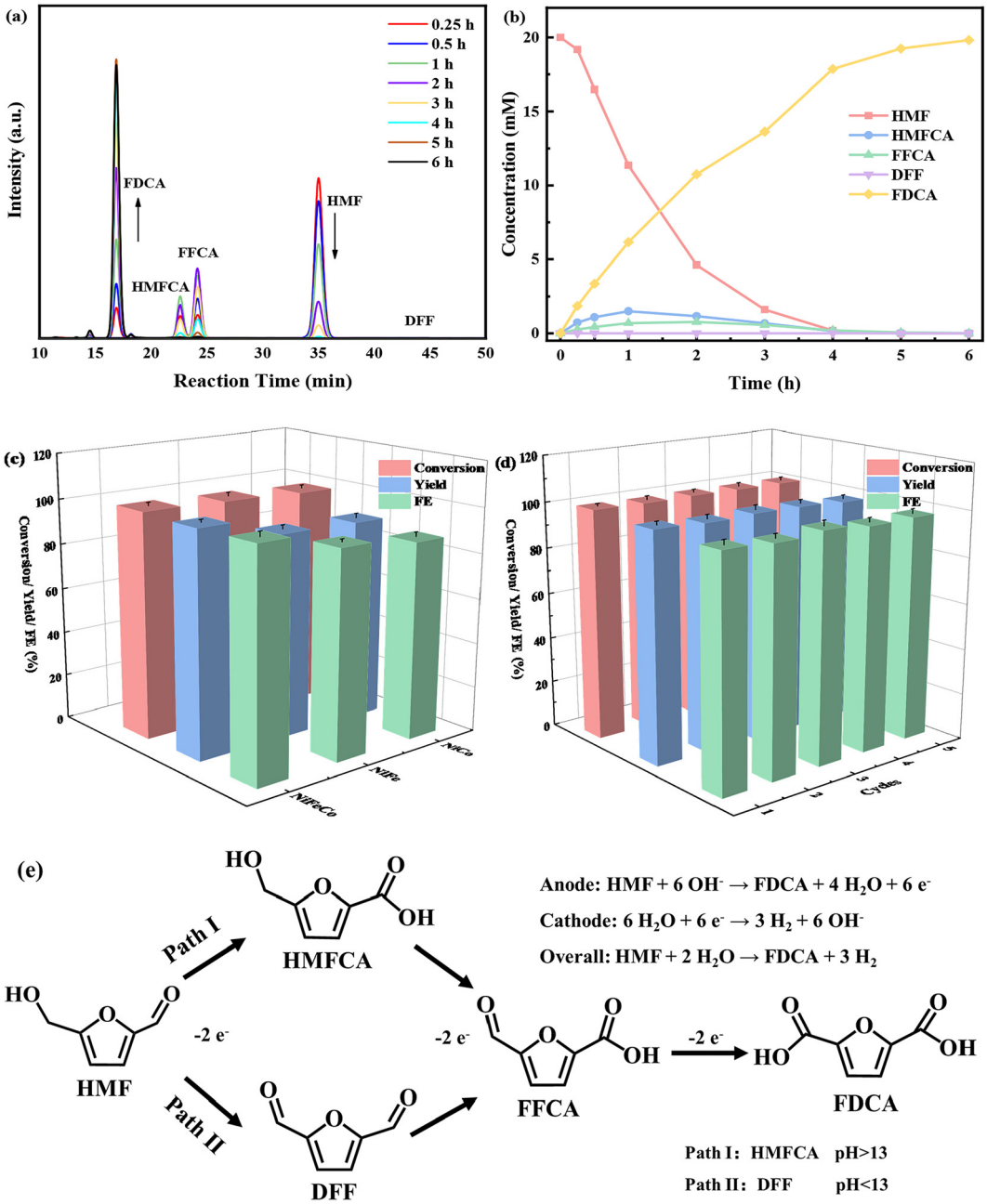

Fig. 4 (a) HPLC chromatograms; (b) concentration change of the substance; (c) HMF conversion, FDCA yield and FE of NiFeCo-LDHs; (d) recycling of NiFeCo-LDHs; and (e) the path of HMF electrooxidation to FDCA.

analysis indicated that the leaching levels of Ni, Fe, and Co were below 2% after each cycle, suggesting that the synthesized hierarchical nanoarrays were stable under the specified reaction conditions.

Hierarchical nanosheet architectures of the NiFeCo-LDHs were observed to be well-maintained after detailed characterization of the employed electrode (Fig. S6b†). The surface element compositions and valence states of the NiFeCo-LDH electrode during HMF oxidation investigated using XPS showed a blue shift along with the Ni^{3+} signal in the Ni 2p of NiFeCo-LDHs (Fig. 5a), which indicated that Ni^{2+} underwent deep oxidation to form β-NiOOH and that Ni^{3+} was generated and participated in the HMF oxidation.[50] As for the contribution of FeCo doping in the active site for HMF oxidation, XPS characterization of the catalyst before and after the reaction showed that the diffraction peak of Ni^{3+} appeared in Ni 2p after the reaction, while the valence states of Fe 2p and Co 2p did not change, so it was preliminarily believed that Fe/CoOOH was not produced during the reaction. The O 1s XPS spectra of the fresh NiFeCo-LDHs (Fig. 5b) showed three distinct O 1s peaks at 529.64 eV, 531.18 eV, and 534.29 eV, which correspond to the binding energies of the adsorbed M–O

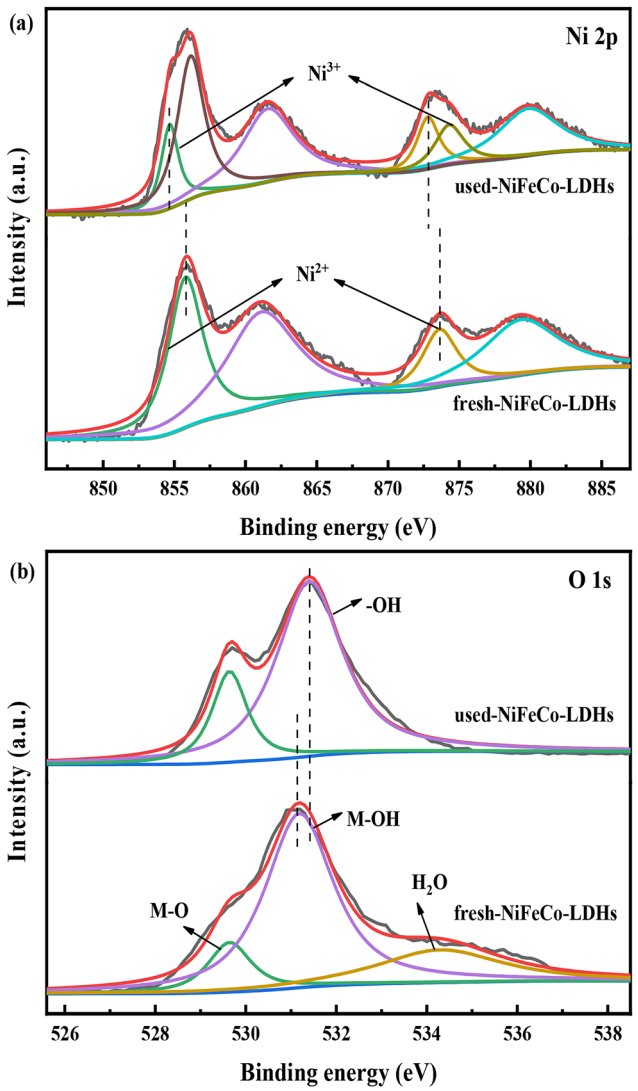

Fig. 5 XPS spectra of the used-NiFeCo-LDH and fresh-NiFeCo-LDH electrodes: (a) Ni 2p and (b) O 1s XPS spectra.

bond, M–OH bond, and H_2O,[51] respectively. The M–OH peak of the used NiFeCo-LDHs was found to exhibit a positive shift of 0.32 eV when compared with fresh NiFeCo-LDHs, indicating that Ni atoms transferred their electrons to O atoms. This indicates that the O atoms in NiFeCo-LDHs have a slight attraction that promotes the electrochemical dehydrogenation process of Ni^{2+} and generates active β-NiOOH substances.[52] The valence states of Co and Fe did not change after electrocatalytic oxidation (Fig. S6c and d†). Therefore, it can be inferred that the Ni site was the main catalytic center for HMF electrocatalytic oxidation, where Co and Fe had an important metal synergistic role with Ni metal.

2.4. Mechanism

The low-valence state of the metal ion was electrochemically oxidized to a higher-valence state (Fig. S7†). The formed high-valence medium (active phase) should activate and cleave the C–H/O–H bond by hydride transfer, and finally cycle back to the low-valence state to regenerate the active phases, while oxidizing HMF to FDCA.[53] The HMFOR in the alkaline system involves the adsorption and coupling of organic molecules and OH^-, but the precise adsorption mechanism is uncertain. Based on previous research,[23,54] the Eley–Rideal (E–R) mechanism is followed when the reaction rate is solely dependent on the adsorption energy, while the Langmuir–Hinshelwood mechanism is followed when both the adsorption energy and the substrate concentration affect the reaction rate[55] (Fig. 6e). To verify the absorption mechanism of the HMFOR on a pre-prepared electrode, a series of CV tests were carried out. By maintaining a concentration of 20 mM HMF and varying the KOH content, the current density and the correlation with the concentration of OH^- were determined and are illustrated in Fig. 6a. The corresponding cyclic voltammetry curves are presented in Fig. S7.† The current density increased as $C_{(OH^-)}$ increased, which indicates that the reaction is part of the L–H mechanism and that the current density is dependent on the KOH concentration. On the other hand, an experiment was carried out in which the KOH concentration remained fixed (Fig. 6b) and the HMF concentration was adjusted and the associated CV curves were measured (Fig. S7†). An increase in the HMF concentration resulted in a current density that initially increased and subsequently declined, which further suggests the importance of substrate concentration to the current density, and that the reaction conforms to the L–H mechanism. In addition, the current density increases with the increase of C (OH^-), which indicates that the high-alkali environment is conducive to maintaining high activity (Fig. S7a†). However, in contrast to the alkaline oxygen evolution reaction (OER), which involves only hydroxide ions (OH^-) as the initial reactant, the typical hydroxy methyl furfural oxidation reaction (HMFOR) process necessitates the co-adsorption of both OH^- and HMF molecules on the catalyst surface, with the former evolving to an electrophilic hydroxyl group ($OH^- \rightarrow OH^* + e^-$) acting as an oxidizing agent.[56] Excessive adsorption of HMF may lead to active sites being occupied on the catalyst, thereby hindering subsequent adsorption of OH^- and resulting in diminished catalytic activity (Fig. S7d†).

In situ Raman spectroscopy was used to investigate how the surface structure of the electrocatalyst evolved during OER and HMFOR (Fig. S7†). The NiFeCo-LDH electrode exhibited two distinct peaks at 438 cm^{-1} and 569 cm^{-1} during the OER, which are attributed to the bending and stretching vibrations of the Ni^{3+}–O bond, indicating that β-NiOOH is synthesized when the applied potential exceeds 1.30 V *vs.* RHE (Fig. 6c).[57] Compared with previous studies (473 and 575 cm^{-1}), the co-doping of Fe and Co resulted in a negative shift of the two peaks associated with the NiOOH species, further demonstrating a synergistic effect between metals. Peaks of β-NiOOH were observed during HMF oxidation, and no diffraction peak of Fe/CoOOH was observed, which confirmed that FeCo doping does not play a role as the active site in HMF oxidation, and that the real active site is NiOOH. However, the peak of β-NiOOH did

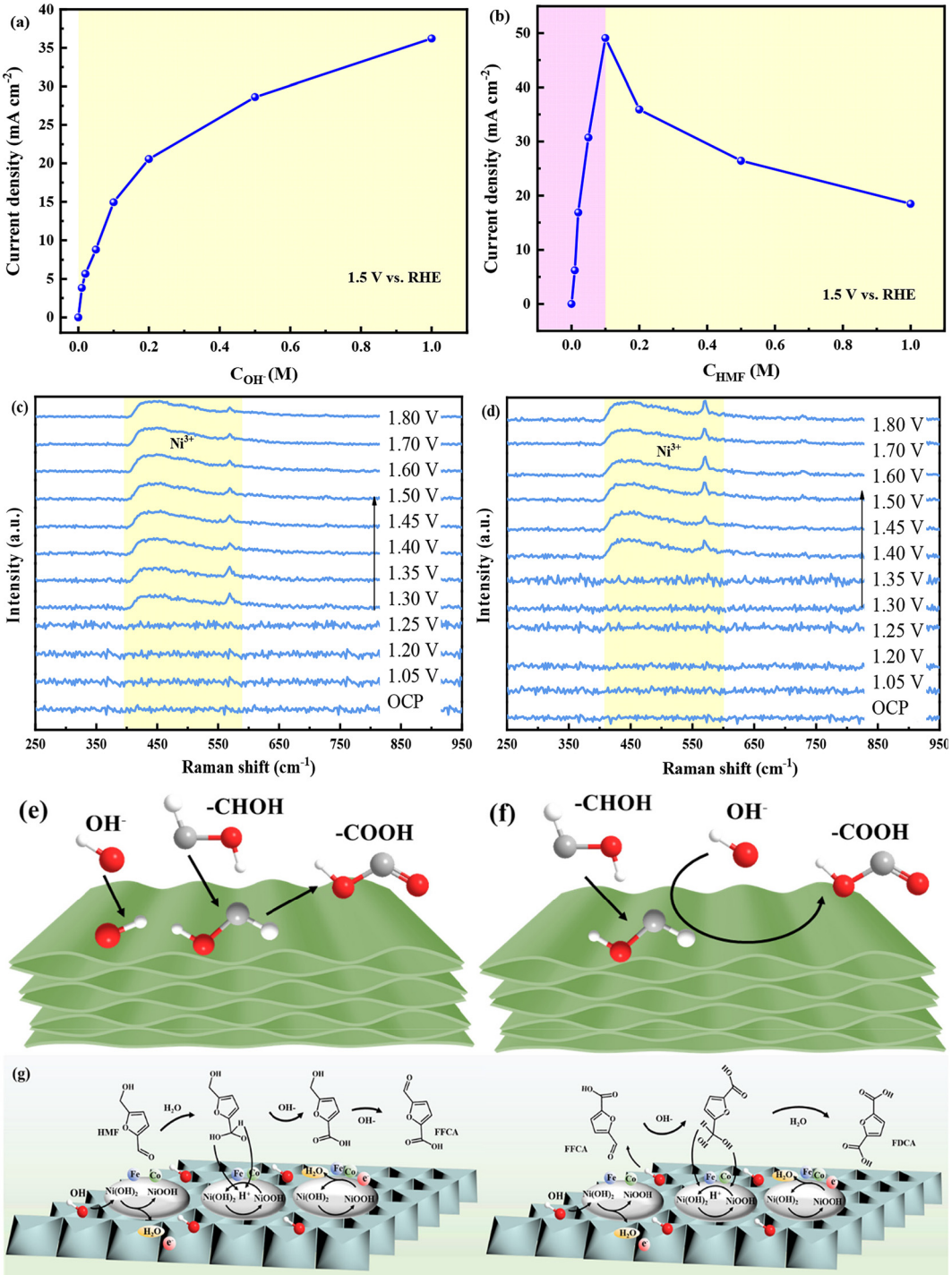

Fig. 6 Relationship between the current density and C_{OH^-} (a) and C_{HMF} (b) at 1.5 V *vs.* RHE; *in situ* Raman spectra of NiFeCo-LDHs for the (c) OER and (d) HMFOR; possible (e) E–R adsorption mode and (f) L–H adsorption mode; and (g) schematic diagram of the catalytic mechanism.

not occur until 1.40 V *vs.* RHE, which means that when HMF is present it can consume the species and inhibit the formation of β-NiOOH.[24] Ni^{3+} was most likely converted into Ni^{2+} by the hydroxy and aldehyde groups in HMF, while HMF was dehydrogenated to the oxidative derivative. Therefore, HMF electrooxidation catalyzed by NiFeCo-LDH electrodes is a traditional indirect oxidation reaction (Fig. 6g and S7†). The specific reaction process is as follows: under the influence of the applied potential, Ni^{2+} loses electrons and undergoes dehydrogenation to form Ni^{3+}. Subsequently, the Ni^{3+}–O bond spontaneously captures protons and electrons from the aldehyde group of HMF. Then, HMF is oxidized to 2,5-furandicar-

boxylic acid (FDCA), and the Ni^{3+}–O bond is then converted to a Ni^{2+}–OH bond. Finally, the Ni^{2+}–OH/Ni^{3+}–O cycle is completed.[58,59] Electrocatalytic oxidation of HMF on the β-Ni $(OH)_2$ surface is proposed to proceed through the following steps:

$$\beta\text{-Ni(OH)}_2 + OH^- \rightarrow \beta\text{-NiOOH} + H_2O + e^-, \quad (1)$$

$$\beta\text{-NiOOH} + HMF \rightarrow FDCA + \beta\text{-Ni(OH)}_2. \quad (2)$$

2.5. DFT calculations

The impact of FeCo co-doping on the catalytic performance of the HMFOR was methodically examined using density functional theory (DFT). The dehydrogenation analysis of the Ni–OH bond showed that the dehydrogenation Gibbs free energy of β-$Ni(OH)_2$ was 6.23 eV (Fig. 7a). The dehydrogenation Gibbs free energies of NiFe-LDHs, NiCo-LDHs, and NiFeCo-LDHs were 6.04 eV, 3.73 eV, and 3.35 eV, respectively. It was demonstrated that the introduction of a second or third metal (Co and Fe) to the NF can significantly reduce the Gibbs free energy. It is suggested that FeCo co-doping can greatly promote dehydrogenation kinetics and aid in the conversion of β-$Ni(OH)_2$ into the active species NiOOH.

The adsorption energy of the catalysts for HMF was investigated (Fig. 7b). The interaction between the metals can alter the adsorption behavior of HMF. NiFeCoOHO has a stronger adsorption energy (E_{ads}) of −1.59 eV than NiFeOHO (−1.36 eV) and NiCoOHO (−1.56 eV), respectively. The electronegativities of Fe (1.83) and Co (1.88) are lower than that of Ni (1.91), which facilitates the adsorption of hydroxyl groups from HMF onto the surface of the catalyst.[60] The O site for surface dehydrogenation and the complex-unsaturated Ni in NiFeCoOHO should bind to the OH^- end and the CHO end of HMF, respectively. The charge density difference for HMF adsorption

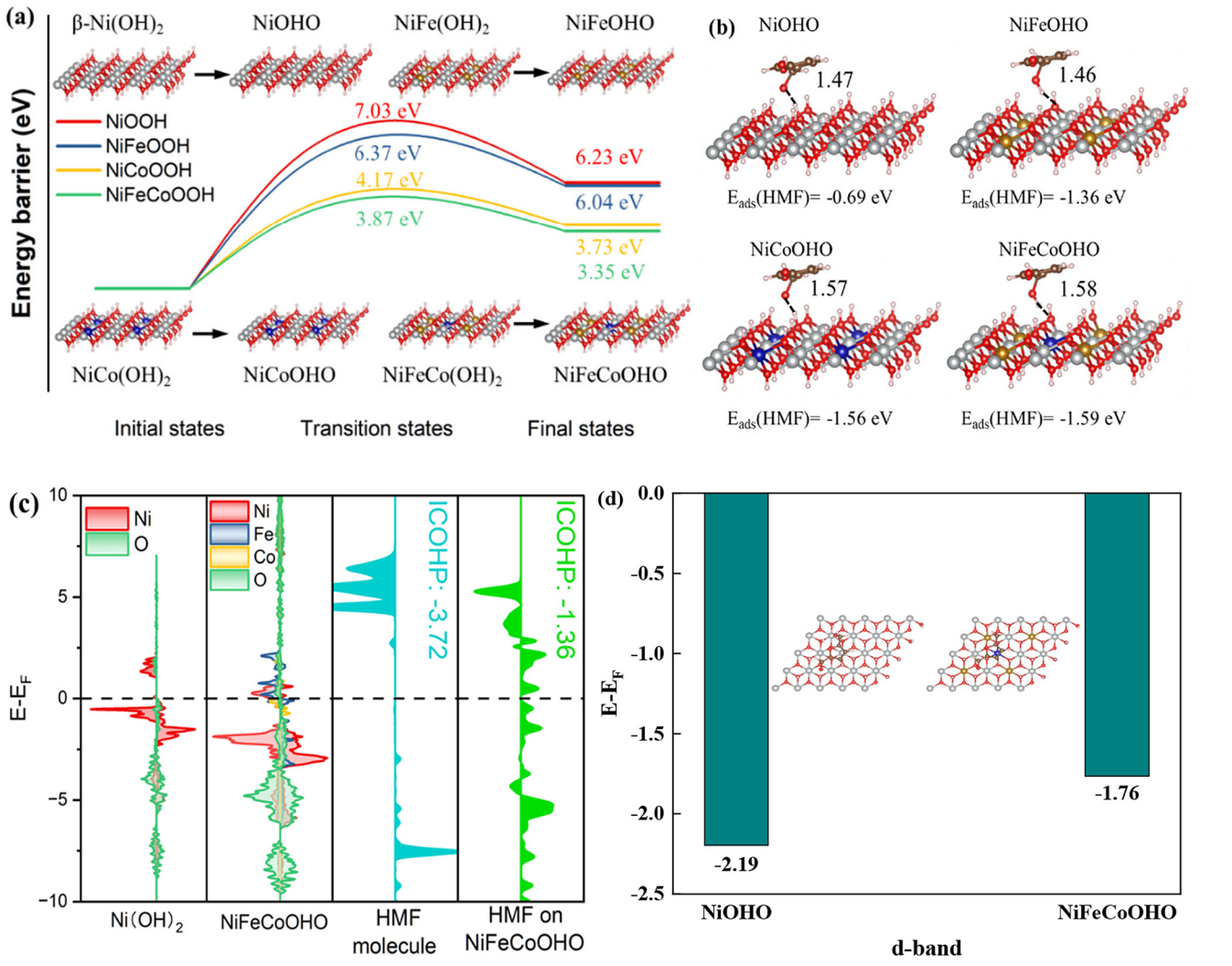

Fig. 7 (a) Dehydrogenation energy profiles of the Ni–OH bond on the $Ni(OH)_2$, Fe, Co-doped and FeCo co-doped electrodes. (b) Models showing side views of HMF adsorption arrangements and the associated adsorption energy. (c) The PDOS and −COHP of HMF adsorption on $Ni(OH)_2$ and NiFeCoOHO. (d) d-band center of NiOHO and NiFeCoOHO. H-bond length (in Å) is labeled. Ni atoms (gray), Fe atoms (yellow), Co atoms (blue), O atoms (red), H atoms (white), and C atoms (brown).

on NiFeCoOHO showed that electron transfer occurred between NiFeCoOHO and the nearby O atoms (Fig. S9†).[61]

The partial density of states (PDOS) of NiFeCoOHO and the crystal orbital Hamilton population (COHP) of HMF molecules adsorbed on NiFeCoOHO were calculated (Fig. 7c). The PDOS of Ni 2p in NiFeCoOHO differs from that in $Ni(OH)_2$ (Fig. 7c), which indicates that the strong electronic interactions resulting from FeCo co-doping have modified the electronic configuration of Ni.[62] Additionally, the 2p orbitals of Fe and Co have strong hybridization with the 2p orbitals of $Ni(OH)_2$, suggesting that Fe and Co have strong binding ability in Ni $(OH)_2$ and thus exhibit good stability. An indication of HMF activation that can be quantified is the integrated COHP (ICOHP) value (Fig. 7c). HMF molecules on NiFeCoOHO sites are activated to different degrees compared to free HMF molecules.[63] The ICOHP of HMF at the NiFeCoOHO site was relatively positive (−1.36 eV), indicating that the O–H bond is weakened after Fe and Co doping. The activated O–H bond facilitates the subsequent oxidation.[64]

The average d-band center value was investigated by DFT calculations to explore the impact of Fe and Co on the electrocatalytic oxidation properties of Ni-based LDHs (Fig. 7d). The d-band center of NiOHO was −2.19, and after FeCo co-doping, the d-band center of the NiFeCoOHO was −1.76. This indicates that the adsorption capacity between the active site and the intermediate is relatively strong, thereby promoting reaction kinetics.[65] With the increase in the d-band center value, the number of electrons replaced by the anti-bond decreases, which will increase the link between the catalyst and the reaction substrate, thus promoting the oxidation reaction.[66] The above experimental and theoretical results confirmed that FeCo co-doping can effectively reduce the reaction energy barrier and activate HMF, thereby improving the yield and selectivity of FDCA.

3. Conclusion

In conclusion, calcination and hydrothermal treatment were employed to generate an effective HMFOR electrocatalyst of hierarchical nanosheet arrays (NiFeCo-LDHs). This approach aimed to investigate the influence of FeCo co-doping and subsequent surface reconstruction on enhancing the performance of Ni electrodes in the HMFOR. At a potential of 1.5 V *vs.* RHE, 100% HMF conversion, 98.7% FDCA yield, and 98% FE were achieved. Electrochemical measurements and *in situ* Raman spectroscopy confirmed that FeCo co-doping adjusted the electronic structure and changed the surface structure of the catalyst. It was found that the evolved β-NiOOH (Ni^{3+}) is the true active center of the HMFOR. β-NiOOH generated by electrocatalysis can effectively capture protons in CHO^- of HMF to achieve electron transfer, which can be regarded as an indirect oxidation reaction. The adsorption characteristics of HMF are consistent with the Langmuir–Hinshelwood mechanism. The DFT calculations further confirmed the critical role of FeCo co-doping in enhancing electron transfer and accelerating the formation of intermediates during the dehydrogenation of Ni(OH)O. Additionally, it was demonstrated that β-NiOOH can effectively capture protons from CHO^- in HMF, thereby facilitating electron transfer and significantly improving the HMFOR. It has been proved that FeCo co-doping can effectively reduce the reaction energy barrier and activate HMF, thereby improving the yield and selectivity of FDCA. These intriguing findings have ramifications for the sensible development of advanced polymetallic site electrocatalysts and their application in the upgrading of biomass derivatives.

Author contributions

All authors contributed to the study conception and design. Material preparation, data collection and analyses were performed by Bingkun Chen, Bowen Yang and Yaqiong Su. The first draft of the manuscript was written by Haixin Guo. It was edited by all authors and critically revised for important intellectual content by Qidong Hou, Richard Lee Smith Jr and Xinhua Qi. All authors read and approved the final manuscript.

Data availability

All data generated or analyzed during this study are included in this published article and its ESI.†

Conflicts of interest

The authors have no relevant financial or non-financial interests to disclose.

Acknowledgements

The authors are grateful for the funding from the Elite Youth Program of the Chinese Academy of Agricultural Sciences (to Haixin Guo), the Mate and Key Laboratory of Technologies and Models for Cyclic Utilization from Agricultural Resources, Ministry of Agriculture and Rural Affairs, P. R. China (KLTMCUAR2023-02) and the National Natural Science Foundation of China (U23A20125).

References

1 J. Zhang, W. Gong, H. Yin, D. Wang, Y. Zhang, H. Zhang, G. Wang and H. Zhao, *ChemSusChem*, 2021, **14**, 2935–2942.
2 B. Zhu, C. Chen, L. Huai, Z. Zhou, L. Wang and J. Zhang, *Appl. Catal., B*, 2021, **297**, 120396.
3 L. Guo, X. Zhang, L. Gan, L. Pan, C. Shi, Z.-F. Huang, X. Zhang and J.-J. Zou, *Adv. Sci.*, 2023, **10**, 5540.
4 B. Chen, Y. Abe, H. Guo and R. Lee Smith, *Fuel*, 2024, **376**, 132745.

5 S. Pandey, M.-J. Dumont, V. Orsat and D. Rodrigue, *Eur. Polym. J.*, 2021, **160**, 110778.
6 J. B. Heo, Y.-S. Lee and C.-H. Chung, *Biotechnol. Adv.*, 2021, **53**, 107838.
7 D. Yan, J. Xin, Q. Zhao, K. Gao, X. Lu, G. Wang and S. Zhang, *Catal. Sci. Technol.*, 2018, **8**, 164–175.
8 R. Li, K. Xiang, Z. Peng, Y. Zou and S. Wang, *Adv. Energy Mater.*, 2021, **11**, 2292.
9 L. Thapa, A. Bhaumik, S. Mondal and C. R. Raj, *J. Mater. Chem. A*, 2023, **11**, 26242–26251.
10 W.-J. Liu, L. Dang, Z. Xu, H.-Q. Yu, S. Jin and G. W. Huber, *ACS Catal.*, 2018, **8**, 5533–5541.
11 C. Wang, H.-J. Bongard, C. Weidenthaler, Y. Wu and F. Schuth, *Chem. Mater.*, 2022, **34**, 3123–3132.
12 M. Zhou, J. Chen and Y. Li, *Catal. Sci. Technol.*, 2022, **12**, 4288–4297.
13 B. Zhang, H. Fu and T. Mu, *Green Chem.*, 2022, **24**, 877–884.
14 D. Tian, S. R. Denny, K. Li, H. Wang, S. Kattel and J. G. Chen, *Chem. Soc. Rev.*, 2021, **50**, 12338–12376.
15 Y. Feng, K. Yang, R. L. L. Smith Jr and X. Qi, *J. Mater. Chem. A*, 2023, **11**, 6375–6383.
16 S. Li, S. Wang, Y. Wang, J. He, K. Li, Y. Xu, M. Wang, S. Zhao, X. Li, X. Zhong and J. Wang, *Adv. Funct. Mater.*, 2023, **33**, 14488.
17 Y. Song, Z. Li, K. Fan, Z. Ren, W. Xie, Y. Yang, M. Shao and M. Wei, *Appl. Catal., B*, 2021, **299**, 120669.
18 Y. Lu, C.-L. Dong, Y.-C. Huang, Y. Zou, Z. Liu, Y. Liu, Y. Li, N. He, J. Shi and S. Wang, *Angew. Chem., Int. Ed.*, 2020, **59**, 19215–19221.
19 B. Liu, S. Xu, M. Zhang, X. Li, D. Decarolis, Y. Liu, Y. Wang, E. K. Gibson, C. R. A. Catlow and K. Yan, *Green Chem.*, 2021, **23**, 4034–4043.
20 X.-Q. Xie, J. Liu, C. Gu, J. Li, Y. Zhao and C.-S. Liu, *J. Energy Chem.*, 2022, **64**, 503–510.
21 C. Liu, X.-R. Shi, K. Yue, P. Wang, K. Zhan, X. Wang, B. Y. Xia and Y. Yan, *Adv. Mater.*, 2023, **35**, 11177.
22 Y. Yang and T. Mu, *Green Chem.*, 2021, **23**, 4228–4254.
23 M. T. Bender, X. Yuan, M. K. Goetz and K.-S. Choi, *ACS Catal.*, 2022, **12**, 12349–12368.
24 B. Zhou, C.-L. Dong, Y.-C. Huang, N. Zhang, Y. Wu, Y. Lu, X. Yue, Z. Xiao, Y. Zou and S. Wang, *J. Energy Chem.*, 2021, **61**, 179–185.
25 H. Bode, K. Dehmelt and J. Witte, *Electrochim. Acta*, 1966, **11**, 1079–1087.
26 A. Van der Ven, D. Morgan, Y. S. Meng and G. Ceder, *J. Electrochem. Soc.*, 2006, **153**, A210–A215.
27 F.-B. Liu, N. Lin, L.-C. Cong, X.-X. Li, F.-Y. Han, D.-Y. Xin and H.-B. Lin, *ChemCatChem*, 2023, **15**, 765.
28 X. Huang, J. Song, M. Hua, Z. Xie, S. Liu, T. Wu, G. Yang and B. Han, *Green Chem.*, 2020, **22**, 843–849.
29 M. Zhang, Y. Liu, B. Liu, Z. Chen, H. Xu and K. Yan, *ACS Catal.*, 2020, **10**, 5179–5189.
30 W. Chen, Y. Wang, B. Wu, J. Shi, Y. Li, L. Xu, C. Xie, W. Zhou, Y.-C. Huang, T. Wang, S. Du, M. Song, D. Wang, C. Chen, J. Zheng, J. Liu, C.-L. Dong, Y. Zou, J. Chen and S. Wang, *Adv. Mater.*, 2022, **34**, 2105320.
31 Y. Zhou, Y. Shen and H. Li, *Appl. Catal., B*, 2022, **317**, 121776.
32 N. Jiang, B. You, R. Boonstra, I. M. T. Rodriguez and Y. Sun, *ACS Energy Lett.*, 2016, **1**, 386–390.
33 J. Zhang, S. Zhang, Z. Zhang, J. Wang, Z. Zhang and G. Cheng, *J. Alloys Compd.*, 2023, **939**, 168753.
34 X. Liu, L. Liao, G. Xia, F. Yu, G. Zhang, M. Shu and H. Wang, *J. Mater. Chem. A*, 2022, **10**, 25047–25054.
35 L. Zhuang, L. Ge, Y. Yang, M. Li, Y. Jia, X. Yao and Z. Zhu, *Adv. Mater.*, 2017, **29**, 1606793.
36 L. Xu, Q. Jiang, Z. Xiao, X. Li, J. Huo, S. Wang and L. Dai, *Angew. Chem., Int. Ed.*, 2016, **55**, 5277–5281.
37 X. Yi, V. Celorrio, H. Zhang, N. Robertson and C. Kirk, *J. Mater. Chem. A*, 2023, **11**, 22275–22287.
38 H.-L. Zhang and F.-J. Wu, *Int. J. Electrochem. Sci.*, 2020, **15**, 7417–7422.
39 G.-X. Tong, F.-T. Liu, W.-H. Wu, J.-P. Shen, X. Hu and Y. Liang, *CrystEngComm*, 2012, **14**, 5963–5973.
40 Y. Wang, X. Luo, W. Lu, B. Huang and Y. Yang, *Langmuir*, 2023, **39**, 423–432.
41 Y. Qian, M. Hu, L. Li, S. Cao, J. Xu, J. Hong, X. Liu, J. Xu and C. Guo, *Fuel*, 2024, **361**, 130653.
42 J. Wu, W. Xie, Y. Zhang, X. Ke, T. Li, H. Fang, Y. Sun, X. Zeng, L. Lin and X. Tang, *J. Energy Chem.*, 2024, **95**, 670–683.
43 C. Liu, X.-R. Shi, K. Yue, P. Wang, K. Zhan, X. Wang, B. Y. Xia and Y. Yan, *Adv. Mater.*, 2023, **35**, 11177.
44 L. Jia, Y. Wang, D. Duan, X. Zhou, S. Liu and Q. Wei, *J. Alloys Compd.*, 2024, **984**, 173974.
45 J. Lian, Y. Wu, Z. Lu and Q. Zang, *Int. J. Hydrogen Energy*, 2023, **48**, 24295–24305.
46 Y. Liu, D. Yang, Z. Liu and J. H. Yang, *J. Power Sources*, 2020, **461**, 228165.
47 M. Pramanik, C. Li, M. Imura, V. Malgras, Y.-M. Kang and Y. Yamauchi, *Small*, 2016, **12**, 1709–1715.
48 L. Gao, X. Wen, S. Liu, D. Qu, Y. Ma, J. Feng, Z. Zhong, H. Guan and L. Niu, *J. Mater. Chem. A*, 2022, **10**, 21135–21141.
49 Z. Zhao, M. Zhu, M. Qu, X. Luo, Q. Hu, X. Shen, W. Zheng, Y. Jia, Q. Sun, J. Chen and H. Zheng, *Chem. Eng. J.*, 2024, **484**, 149768.
50 B. J. Taitt, D.-H. Nam and K.-S. Choi, *ACS Catal.*, 2019, **9**, 660–670.
51 Q. Qian, Y. Li, Y. Liu, L. Yu and G. Zhang, *Adv. Mater.*, 2019, **31**, 1139.
52 X. Liu, R. Wang, M. Wei, X. Wang, J. Qiu, J. Zhang, S. Li and Y. Chen, *J. Colloid Interface Sci.*, 2024, **657**, 438–448.
53 Y. Sun, H. Shin, F. Wang, B. Tian, C.-W. Chiang, S. Liu, X. Li, Y. Wang, L. Tang, W. A. Goddard, III and M. Ding, *J. Am. Chem. Soc.*, 2022, **144**, 15185–15192.
54 A. S. May, S. M. Watt and E. J. Biddinger, *React. Chem. Eng.*, 2021, **6**, 2075–2086.
55 W. Chen, C. Xie, Y. Wang, Y. Zou, C.-L. Dong, Y.-C. Huang, Z. Xiao, Z. Wei, S. Du, C. Chen, B. Zhou, J. Ma and S. Wang, *Chem*, 2020, **6**, 2974–2993.
56 X. Xia, J. Xu, X. Yu, J. Yang, A.-Z. Li, K. Ji, L. Li, M. Ma, Q. Shao, R. Ge and H. Duan, *Sci. Bull.*, 2024, **69**, 2870–2880.

57 S. Fan, B. Zhu, X. Yu, Y. Gao, W. Xie, Y. Yang, J. Zhang and C. Chen, *J. Energy Chem.*, 2024, **92**, 1–7.
58 S. Lee, Y.-C. Chu, L. Bai, H. M. Chen and X. Hu, *Chem. Catal.*, 2023, **3**, 100475.
59 R. Luo, Y. Li, L. Xing, N. Wang, R. Zhong, Z. Qian, C. Du, G. Yin, Y. Wang and L. Du, *Appl. Catal., B*, 2022, **311**, 121357.
60 Y. Li, M. Yuan, H. Yang, K. Shi, Z. Sun, H. Li, C. Nan and G. Sun, *Appl. Catal., B*, 2023, **323**, 122167.
61 Y. Wei, J. Huang, H. Chen, S.-J. Zheng, R.-W. Huang, X.-Y. Dong, L.-K. Li, A. Cao, J. Cai and S.-Q. Zang, *Adv. Mater.*, 2024, **36**, 4774.
62 W. Jia, B. Liu, R. Gong, X. Bian, S. Du, S. Ma, Z. Song, Z. Ren and Z. Chen, *Small*, 2023, **19**, 2025.
63 H. Cao, B. Liang, S. Ye, Z. Zhuang, L. Zheng, W. Chen, W. Chen, J. Zhang, Q. Zhang, J. Liu, X. Yan and Q. Zhang, *Chem. Eng. J.*, 2024, **490**, 151883.
64 R. Nelson, C. Ertural, J. George, V. L. Deringer, G. Hautier and R. Dronskowski, *J. Comput. Chem.*, 2020, **41**, 1931–1940.
65 M. Sun, B. Yang, J. Yan, Y. Zhou, Z. Huang, N. Zhang, R. Mo and R. Ma, *Nanoscale*, 2024, **16**, 10618–10627.
66 Y. Li, M. Yuan, H. Yang, K. Shi, Z. Sun, H. Li, C. Nan and G. Sun, *Appl. Catal., B*, 2023, **323**, 122167.